NUCL SCI TECH (2020) 31:11
https://doi.org/10.1007/s41365-019-0716-x

Simulation and prototype testing of multi-wire drift chamber arrays for the CEE

Li-Ming Lyu[1] · Han Yi[1] · Li-Min Duan[2] · Zhao Zhang[1] · Zhi-Gang Xiao[1]

Received: 12 February 2019 / Revised: 1 October 2019 / Accepted: 5 November 2019 / Published online: 3 January 2020

Abstract The building of a large-scale external-target experiment, abbreviated as CEE, in the cooling storage ring at the Heavy Ion Research Facility in Lanzhou has been planned. The CEE is a multi-purpose spectrometer that will be used for various studies on heavy-ion collisions. A multi-wire drift chamber (MWDC) array is the forward tracking detector of the CEE. In this work, GEANT4 simulations were performed for the MWDC forward tracking array with a focus on the track reconstruction algorithm. Combined with the time of flight information, particle identification is achieved. The residue is about 30 μm, while the tracking efficiency is higher than 90% with the current redundancy. In addition, a prototype of the forward tracking system using three MWDCs was assembled and tested using a high-energy proton beam. The firing efficiency of the detector and the reconstruction accuracy of the prototype were derived. The track residue for the protons at about 400 MeV/c is better than 300 μm, meeting the requirements of the CEE. Suggestions for improving the performance of the forward tracking system are given.

Keywords CEE · Multi-wire drift chamber array · Track finding and reconstruction

This work was supported by the National Basic Research Program of China (973) (No. 2015CB856903) and the National Science Foundation of China (No. U1332207).

✉ Li-Ming Lyu
llm12@mails.tsinghua.edu.cn

1 Department of Physics, Tsinghua University, Beijing 100084, China

2 Institute of Modern Physics, Chinese Academy of Sciences, Lanzhou 730000, China

1 Introduction

At present, research on the equation of state of nuclear matter and the phase diagram of the strong interaction matter at high net-baryon number density are drawing increasingly intensive attention. The heavy-ion collision at intermediate and high energies is an important means to explore this field. The cooling storage ring (CSR) at the Heavy Ion Research Facility in Lanzhou (HIRFL) [1] can provide full ion beams of many elements from carbon to uranium with energies of up to 1 GeV/u and is an important scientific device for the studies of high-energy nuclear physics if equipped with an advanced detector.

The existence of a critical end point (CEP) of the first-order phase transition between the quark–gluon plasma (QGP) phase and the hadron phase has been widely investigated [2]. It is believed that the CEP manifests itself by an oscillation behavior of the high-order cumulants of the distribution of certain conserved quantity as a function of the system's energy $\sqrt{s}$ [3]. The experimental non-monotonous distribution of the net proton $\kappa\sigma^2$ has been reported in the first phase beam energy scan (BES-I) program of the STAR collaboration [4]. However, the dropping tail of the oscillation at the low energy side has not yet been confirmed and is one of the scientific goals of various heavy-ion facilities, including the FAIR (Germany), NICA (Russia), and HIAF (China). Recently, various calculations have suggested that the CEP is in the range of $T \sim 110$ MeV and $\mu_B \sim 600$ MeV [5], which can be reached in the beam energy at several GeV/u in fixed-target experiments. Thus, measurements in the energy region of the HIRFL-CSR and HIAF are of significant interest.

The nuclear symmetry energy, i.e., the isovector sector in the equation of state of nuclear matter in hadron phase has recently become a frontier in astrophysics and nuclear physics [6–11], particularly after the GW170817 event [12, 13], for which the density dependence of the symmetry energy was an essential quantity to characterize the tidal deformation of the two merging neutron stars [14–16]. To study the symmetry energy at about $2\rho_0$ in terrestrial laboratories, heavy-ion collisions at sub-GeV/u are favorable. Both experiments and transport model simulations have shown that the fireball formed in heavy-ion collisions experiences the largest space-time volume and nuclear stopping power in this energy region [17–19]. Therefore, the sensitivity of the observables on the nuclear equation of state at about $2\rho_0$ is optimized [19]. For these purposes, as well as others, a large-scale multi-purpose spectrometer, abbreviated as CEE [20], was proposed at the HIRFL-CSR with the flexibility to continue running on future HIAF.

Before construction, it is necessary to verify that the design of the spectrometer meets the requirements of physical research through full simulations and prototype tests. So far, many R&D works have been conducted for the subsystems, including the time projection chamber (TPC) [21] and time of flight (TOF) detectors [22–28], multi-wire drift chambers (MWDCs) [20, 29–31, 31], beam monitor [32], and readout electronics [33–36]. In the current conceptual design [20], the forward tracking system consists of two arms of MWDC arrays followed by a TOF wall (eTOF) made of a multilayer-resistive plate counter (MRPC) to measure the charged particles at forward rapidity. Each arm consists of three MWDCs plus one MRPC wall. In this article, the simulation studies and prototype tests of the forward tracking MWDC array are reported. Section 2 presents the simulation studies with a focus on the track reconstruction; Sect. 3 presents the results of the beam test of a large area MWDC array prototype; and Sect. 4 presents a summary of this study.

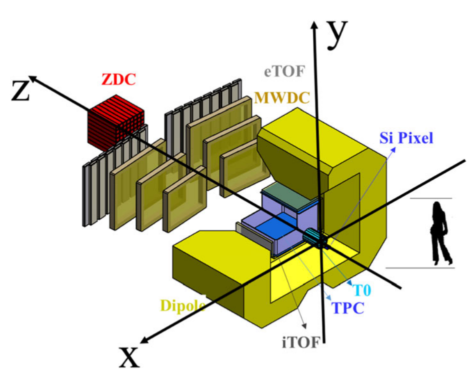

Fig. 1 (Color online) Schematic diagram of the CEE [20]

2 Simulation study

Figure 1 shows the conceptual design of the CEE [20]. The CEE includes several subsystems. The main component is a large acceptance dipole providing the magnetic field to bend the charged particles. Inside the dipole is a TPC recording the trajectories of the charged particles bent by the magnetic field and delivering the momentum information of the particles. Two complanate MRPCs are installed on the left and right side of the TPC, the so-called inner TOF wall (iTOF), to measure the TOF and further provide particle identification. The TPC and the iTOF cover the mid-rapidity region. On the downstream side of the dipole, two arms of an MWDC array followed by a TOF and an eTOF provide the measurement of the charged particles at forward rapidity, covering the polar angle range of $\theta < 30^{\circ}$ in the laboratory. A silicon pixel detector, called the top metal pixel detector, is installed close to the target at the upstream side of the target to provide the incident position of the beam. A barrel of MRPC arrays surrounds the target covering the large rapidity region to measure the light charged particles and provide a start timing signal [22]. A zero-degree hadron calorimeter (ZDC) is installed far at the downstream side of the target to measure the collision centrality.

The MWDC is developed on the basis of the multi-wire proportional chamber (MWPC) [37]. Field wires are added between the signal wires to modulate the electric field and to form drift cells near each signal wire. With the appropriate working gas, the drift velocity of the electrons in the drift cell is substantially uniform, and the drift distance can be determined from the drift time. Compared with the MWPC, the number of signal wires and readout electronic devices is much smaller. For the detailed structure of the drift cell of the CEE MWDC, we refer readers to [31].

2.1 Model construction with GEANT4

GEANT4 is a Monte Carlo simulation software widely used in the field of nuclear physics and particle physics [38]. Because we concentrate on the simulation of the MWDC array, only the magnetic dipole with a detailed field map, the MWDC array, and the eTOF wall are constructed based on GEANT4, as shown in Fig. 2. The gap size is $180\,(L) \times 220\,(W) \times 100\,(H)\,\mathrm{cm}^3$, the volume size of the homogeneous field (1% variance) is $100\,(L) \times 110\,(W) \times 80\,(H)\,\mathrm{cm}^3$. The other geometric information can be found in [20]. The field is calculated in parallel with the design of the dipole. The field map is shown in Fig. 3. Here, the z-direction is defined as the beam direction, and the y-direction is defined as the vertical direction, as shown in Fig. 1. The field in the vicinity of the

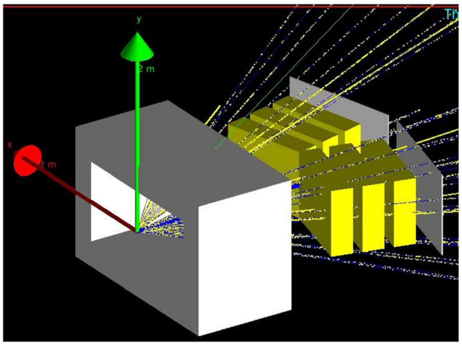

Fig. 2 (Color online) Forward tracking system and dipole of the CEE constructed with GEANT4

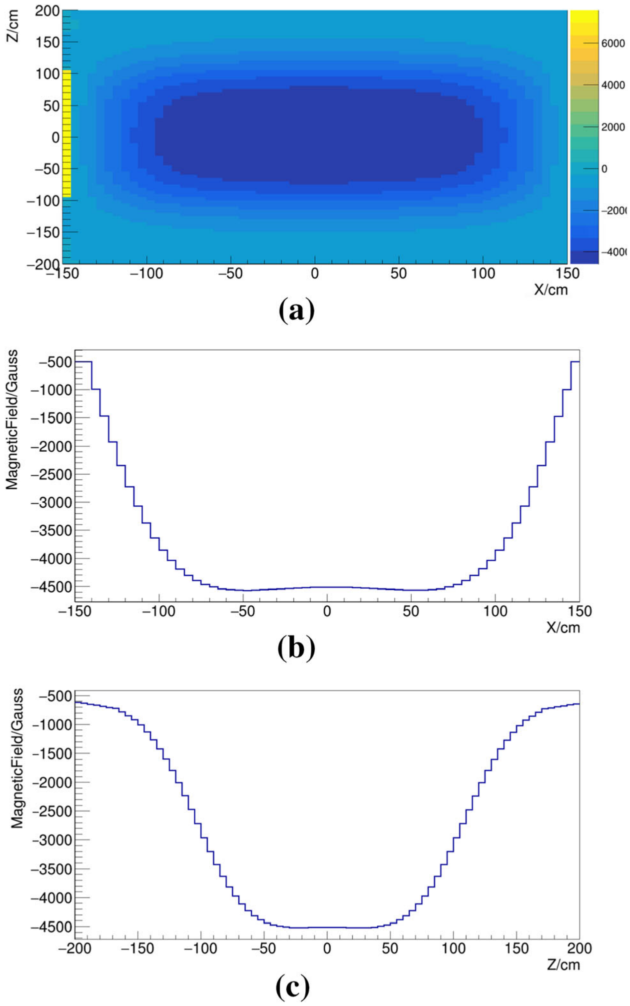

Fig. 3 (Color online) Two-dimensional magnetic field distribution (**a**); the projection of the field of B_y at $z = 0$ (**b**); and projection of the field of B_y at $x = 0$ (**c**)

first layer of the MWDC closest to the dipole is at the level of 500 G, which is about 10% of the central region and is ignored in the tracking procedure.

The event generator is designed based on the experimental data of heavy-ion collisions in the same energy region. As the output of the generator, the multiplicity and phase-space distribution of the particles, including pions, protons, and light charged particles, is linearly interpolated from the phase-space distribution of the same species measured in C+C, Ni+Ni, and Au+Au at beam energies from 400 to 1200 MeV/u [39]. Because the yields and width of the rapidity distribution vary monotonously with the beam energy and with of the system's size, respectively, both longitudinally and transversely, the interpolation generates a nearly true phase distribution of the charged products in the CSR energy region. This method can circumvent the deficiency of the transport model, which usually overestimates the nucleon yield while underestimating the yield of clusters. An energy of 600 MeV/u is selected because it is the typical energy of the CEE in the HIRCL-CSR. The trajectories of the charged particles originating from the collision at the target position in the magnetic field are tracked. The responses of the MWDC and the eTOF wall are simulated by recording the energy deposition and firing position in the sensitive volume of the detector. The digitized data mainly include the ID of the fired wires, the drift radius, and the energy loss in the corresponding drift cell and the timing when the hit appears in the eTOF wall.

2.2 Track finding and reconstruction based on simulation data

As shown in Fig. 4, the drift chamber used in this work consists of three layers of wires in different orientations. The first layer is vertical (X orientation), and the second and third layers are rotated clockwise and counterclockwise by 30 degrees (U and V orientations, respectively). The normal planes perpendicular to these three orientations are marked as the $X_{\perp}$, $U_{\perp}$, and $V_{\perp}$, respectively. The distance between two adjacent layers is 4 cm, and the size of one drift cell is 1 cm $\times$ 1 cm.

Based on the simulation data, an algorithm for track finding and track reconstruction was developed. In general, track finding and reconstruction can be processed in the following steps depending on the specific geometric characteristics of the detector used [40].

1. Hit information recognition: The hit spatial coordinates and signal heights are extracted from the original digitized fire information based on the geometric database of the detector.
2. Local pattern recognition: In each detector, various hits that may belong to the same track are recognized.

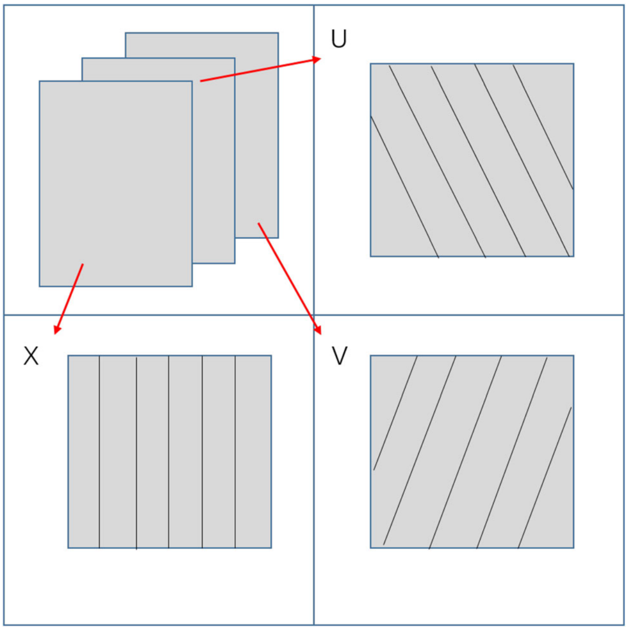

Fig. 4 (Color online) *XUV* sense wire direction of multi-wire drift chamber. The planes perpendicular to the X, U, and V wires are denoted as $X_{\perp}$, $U_{\perp}$, and $V_{\perp}$, respectively

3. Global pattern recognition: The track elements found in the local pattern recognition stage are combined into candidate tracks.
4. Track fitting: The candidate tracks are fitted. If the fitting quality meets our accuracy requirement, it is considered to be a real track; otherwise, the candidate is rejected and released to the data for the next iteration of finding and fitting.

Figure 5a describes how the hit is recognized in the local pattern recognition stage. Three different directions of the fired wires of the same drift chamber are considered to form an isosceles triangle using the geometry of the detector. The red lines in the left panel represent the wire recording a fire, and the black dots represent the approximate original position of the hit on the wire plane. If the base length d of this triangle is less than a specific threshold value (65 mm in this work), the three wires are considered to form a hit. This value is related to the MWDC parameters. We used tracks of simulation data to accumulate this value, which can cover more than 95% of the events. Following this recognition, several hits can be found in each single drift chamber. Figure 5b presents a schematic of the global pattern recognition procedure. The red dotted line in the figure represents the plane in a certain direction in each drift chamber, the black dot (the geometric center of the triangle) represents the hit found in the local pattern recognition in the corresponding chamber. We fit each combination (linear fit) of two hits from the first two chambers in a given plane and prolong the fit to the third plane to match the third hit. As shown by the solid black line, if the distance of the hit in the third chamber to the intersection is within a certain window, the three hits are considered to form a candidate track; otherwise the finding procedure goes to the next iteration of hit candidate recognition. At this stage, the algorithm aims at approximately assigning the hits to a certain track; thus, the drift time and drift length information are not used, and only the geometric characteristics of the fired wire are considered.

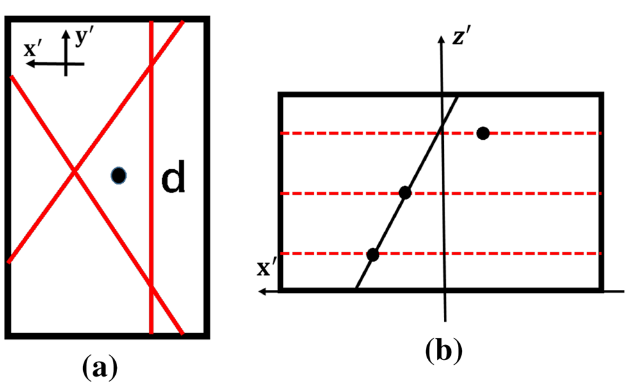

Fig. 5 (Color online) Schematic view of the local (**a**) and global (**b**) pattern recognition

In the fitting phase, the fitting process is divided into two steps, which are fitted using the least squares method, and the drift length is carefully considered.

1. Two-dimensional fitting: This step is performed to fit the track in each $U_{\perp}$, $X_{\perp}$, and $V_{\perp}$ plane. Figure 6 depicts the three drift signals in a single plane. Considering the $X_{\perp}$ plane as an example, fitting the candidate track in this plane is equivalent to finding the common tangent line of three circles. This procedure can be derived analytically, assuming that the line is approximately perpendicular to the sense wire plane. Under this assumption, if we construct

$$\chi^2 = \Sigma_i \left(\frac{|kx'_i + b - z'_i|}{\sqrt{k^2+1}} - r_i \right)^2, \qquad (1)$$

the fitting procedure actually searches the values in the vicinity of minimum χ^2. Here, the Z' direction refers to the direction perpendicular to the MWDC plane. The slope k

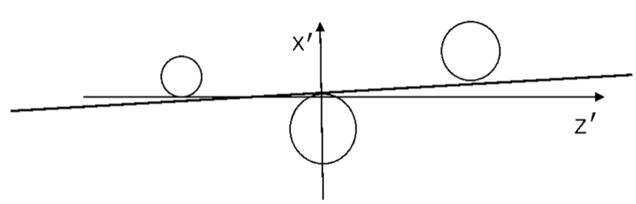

Fig. 6 Two-dimensional fitting to three circles with the radius being the drift length recorded on each individual wire

and the intercept b , assuming they are small enough, can be deduced by

$$\begin{cases} b = \dfrac{z_2' + (r_1 + r_2 + r_3)\sqrt{k^2+1}}{3} \\ k = \dfrac{x_2' z_2' + (x_1' r_1 + x_2' r_2 + x_3' r_3)}{(x_1'^2 + x_2'^2 + x_3'^2) - 3b^2 - z_2'^2 - 2z_2' b + b(r_1 + r_2 + r_3) - r_2 z_2'} \end{cases}, \tag{2}$$

where r_i $(i = 1, 2, 3)$ is the radius of each circle, and (x_i', z_i') $(i = 1, 2, 3)$ are the coordinates of the center of each circle in the local coordinate system fixed to the MWDC plane. It should be pointed out that the assumption that the slope and the intercept of the common tangent are small enough can always be met by coordinate transformation.

After the two-dimensional fitting procedure in all three planes, the fitted lines are used as the initial condition in the three-dimensional fitting, as described below.

2. Three-dimensional fitting: The function of the line in three-dimensional space is fitted to obtain the real track. Here, we assume that the residual magnetic fields in the locations of the MWDCs are negligible and the track forms a straight line penetrating the MWDCs, which can be expressed as [41]

$$\begin{cases} x' = az' + b \\ y' = cz' + d \end{cases}. \tag{3}$$

In the ideal case, this track is identical to the three lines given by the two-dimension fitting in the three planes $U_\perp$, $X_\perp$, and $V_\perp$. In reality, however, the three lines do not necessarily coincide perfectly; thus, the real track is again a fitted line in the three-dimensional coordinate space minimizing

$$\chi^2 = \Sigma_i \frac{[x_i' - (a\cos\alpha_i + c\sin\alpha_i)z_i' - (b\cos\alpha_i + d\sin\alpha_i)]^2}{1 + (a\cos\alpha_i + c\sin\alpha_i)^2}, \tag{4}$$

where α_i is the angle between the wire and the vertical direction. Taking the partial derivative of χ^2 with respect to the parameters a, b, c, d and ignoring the high-order small quantity, one obtains

$$\begin{cases} \Sigma_i z_i'^2(\cos\alpha_i)^2 a + z_i'(\cos\alpha_i)^2 b + z_i'^2\sin\alpha_i\cos\alpha_i c + z_i'\sin\alpha_i\cos\alpha_i d - x_i' z_i'\cos\alpha_i = 0 \\ \Sigma_i z_i'(\cos\alpha_i)^2 a + (\cos\alpha_i)^2 b + z_i'\sin\alpha_i\cos\alpha_i c + \sin\alpha_i\cos\alpha_i d - x_i'\cos\alpha_i = 0 \\ \Sigma_i z_i'^2\sin\alpha_i\cos\alpha_i a + z_i'\sin\alpha_i\cos\alpha_i b + z_i'^2(\sin\alpha_i)^2 c + z_i'^2(\sin\alpha_i)^2 d - x_i' z_i'\sin\alpha_i = 0 \\ \Sigma_i z_i'\sin\alpha_i\cos\alpha_i a + \sin\alpha_i\cos\alpha_i b + z_i'(\sin\alpha_i)^2 c + (\sin\alpha_i)^2 d - x_i'\sin\alpha_i = 0 \end{cases}, \tag{5}$$

where a, b, c, d are the parameters of the line in which the track is located; x_i' and z_i' $(i = 1 - 9)$ are the intersection coordinates of the perpendicular line and the circle, respectively, where the perpendicular line extends from the point where the wire is located to the line obtained by two-dimensional fitting, and the circle is centered at the location of the fired wire and has a radius equal to the drift length, as depicted in Fig. 7.

Figure 8 presents the distribution of the tracking reside, defined as the difference between the drift length and the distance from the wire to the track in each $X_\perp$, $U_\perp$, and $V_\perp$ plane. The results are accumulated for 8985 tracks containing all the light charged particles from the simulated data. Through a double Gaussian fitting, we obtain an average root mean square (RMS) of the residual distribution of 29 μm. It should be pointed out that this result includes the effects of multiple scattering in air and other materials of the detectors, treated automatically in the simulation. The uncertainties caused by the detection are not considered. To check the track finding efficiency in a high multiplicity environment, we simulated 500 events randomly with each event containing ten tracks. It was found that, with the current track finding procedure, more than 90% of the tracks can be reconstructed, and the residue is not deteriorated.

2.3 Momentum reconstruction and particle identification

The final step is the reconstruction of the particle momentum with the magnetic field. We developed a track reversal algorithm that does not require an ideal homogeneity of the field. The particle is reversely incident into the magnetic field along the reconstructed linear track. The deflection in the magnetic field is calculated step by step until the track passes through the transverse plane *o-xy* at the target position. The ratio of momentum to charge, p / q (the charge is fixed at 1 in this work), is iteratively adjusted according to the position of the particle relative to the target. The iteration is ceased when the particle hits the target point within a given precision, taken as the beam spot size (10 mm in this work). In order to make achieve fast iteration and a reasonable momentum, the initial value of the momentum is calculated analytically by assuming that the magnetic field is uniform in the area of the dipole in the y-direction. Figure 9 shows the projection of the track in the XZ plane. The red dot represents the target

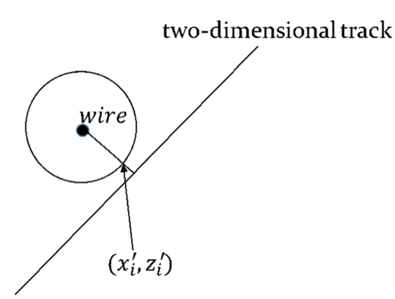

Fig. 7 The position relationship of a fitted track and a drift circle. The cross point (x_i', z_i') is marked

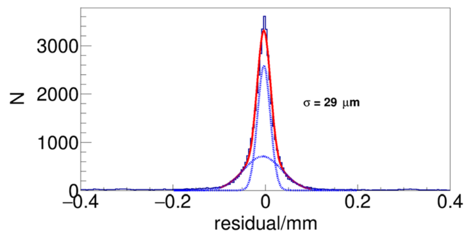

Fig. 8 (Color online) Tracking reside distribution in GEANT4 simulation and reconstruction. The blue dotted curves are the two Gaussian fits and the solid red curve is the sum

point; the black frame is the magnetic field region; the solid red line is the reconstructed track in the form of a straight line from the MWDC array measurement, and the red dotted line is the extension of the track into the magnetic field. The solid blue and green lines represent the position where the track is reversed to the *o-xy* plane with a particle momentum being too small or too large, respectively.

In the case where the deflection angle dθ of each step is sufficiently small, a sufficiently small step size can be obtained, as shown in Fig. 10. The magnetic field will change the position and the direction of the momentum of the moving charged particles. Considering the momentum in the x-direction and the magnetic field in the y-direction as an example, the displacement in the z-direction is

$$dz = r_{P_xB_y} d\theta \frac{d\theta}{2}, \tag{6}$$

and the displacement in the x-direction is

$$dx = r_{P_xB_y} d\theta \left(1 - \frac{d\theta^2}{8}\right), \tag{7}$$

the momentum change in the z-direction is

$$dP_Z = P_X d\theta. \tag{8}$$

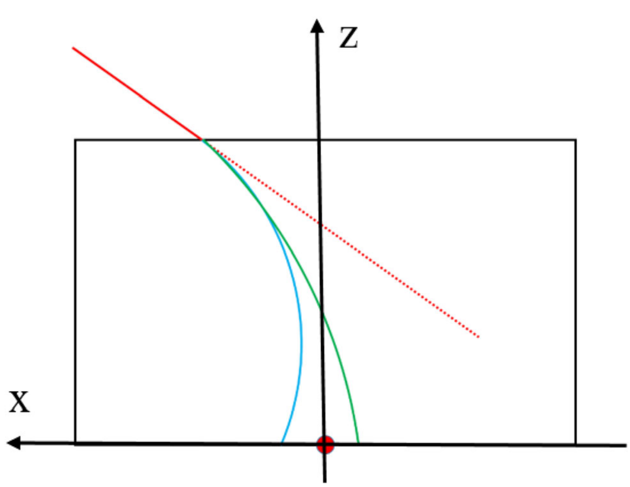

Fig. 9 (Color online) Schematic view of the track reversal algorithm in momentum reconstruction

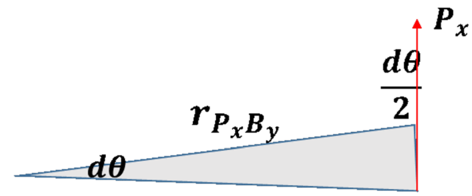

Fig. 10 (Color online) The momentum in the x-direction produces a displacement and the momentum direction changes under the action of the magnetic field B_Y in the y-direction

The displacement and change in the direction of the momentum produced by the momentum in other directions under the action of the magnetic field can be obtained similarly. The displacement and change in the direction of the momentum are accumulated to obtain a change in the position and direction of the movement in one sufficiently small step.

In the case of a detector array with a spatial resolution of 29 μm, the beam spot size is assumed to be 10 mm. The difference between the reconstructed momentum and the Monte Carlo truth track momentum is shown in Fig. 11. Here, 300 μm hit position residues and a TOF resolution of 60 ps are incorporated in the simulation. It is shown that the final momentum resolution is 4%. Using this momentum resolution and taking into account a TOF resolution of about 60 ps, one can arrive at a clear particle identification, as shown in Fig. 12, where the events of Sn+Sn at 600 MeV/u are used.

3 Experimental study

3.1 Experimental situation

In order to further verify the feasibility of the forward tracking system of the CEE, a prototype system was built. As shown in Fig. 13, the system consists of three drift chambers with a sensitive area of 40 × 40 cm^2. The distance between two contiguous signal wires of the same layer is 20 mm, which is also the distance between two

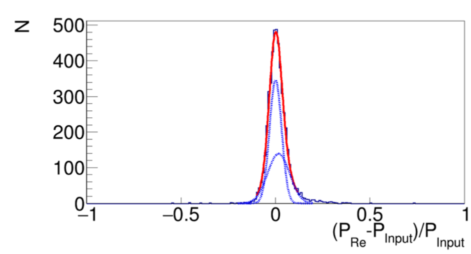

Fig. 11 (Color online) Momentum resolution defined by the error between the Monte Carlo truth input and the reconstruction value. The blue dotted curves are the two Gaussian fits and the solid red curve is the sum

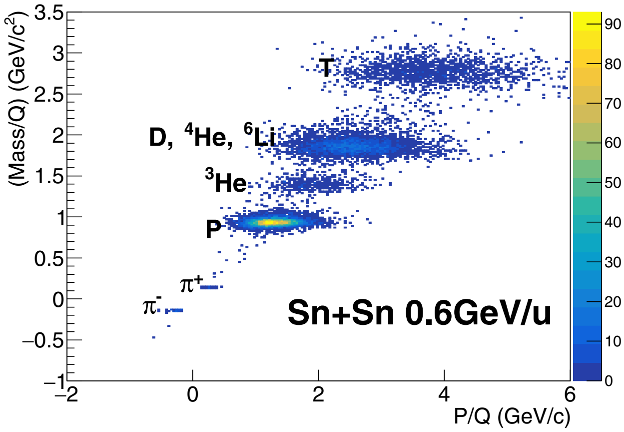

Fig. 12 (Color online) Particle identification achieved in GEANT4 simulation, considering 300 µm tracking residues and a TOF resolution of 60 ps. [20]

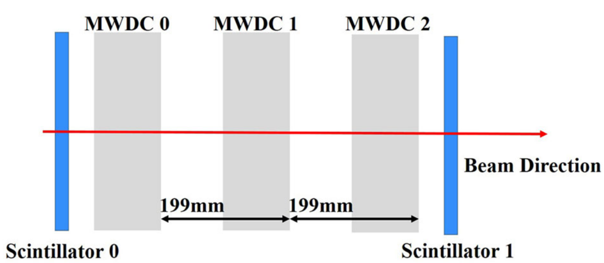

(a)

(b)

Fig. 13 (Color online) Schematic view of the prototype system (**a**), and the prototype system mounted for the beam test (**b**)

contiguous layers. The distance between two contiguous drift chambers is 199 mm. Two plastic scintillators with sizes of $500 \times 150 \times 15$ mm^3 in front of and behind the drift chamber array, respectively, are installed to provide the start timing of the track and to trigger the data acquisition. The entire unit is installed on a rigid aluminum frame.

The working gas of the drift chamber is a mixture of argon (90%) and carbon dioxide(10%). The preamplifier is designed based on a current-amplification scheme [42], and the data acquisition system is based on flash ADC [43] requiring a trigger signal from the coincidence of the four PMT signals of the scintillators.

The beam test of the prototype was carried out in the E3 test beam at the Institute of High Energy Physics, Chinese Academy of Science. The incident beam is generated by a 2.5 GeV primary electron beam hitting a Beryllium target. The momentum of the secondary beams, which are mixed mainly with protons, pions, and very few mixed events, are selected by a magnetic dipole behind the primary target station. The beam used in the prototype test has a momentum of 400 MeV/c or 500 MeV/c, and a count rate of about 100/min.

3.2 Analysis and discussion of results

Figure 14 presents the correlation between the TOF and the energy loss measured by the two scintillators, with only a few components presented. The TOF is recorded by the two scintillators. Several components are visible in the plot. The two main peaks are produced by protons and pions. Pions are situated in the region with very small energy loss for the minimum ionization feature. Figure 15 depicts the correlations between the energies in the two plastic scintillators. Pions and protons with similar P/Q can be seen in the plot, as well as the two-proton events with very small P/Q. The random coincidence between the single proton and double protons are visible. By imposing a window cut on the two plots, the pure single proton events can be selected. As a result, with a total of 155,525 events, we obtained 102,127 single proton events. With these selected one-proton events, one can count the multiplicity of the fired wires M_{W} in each layer, as shown in Fig. 16. Clearly, with the clean one-proton events, the multiplicity distribution peaks at 1. An extension to $M_{\mathrm{W}} > 1$ is visible, indicating that, in some layers, the neighboring wires may also be fired simultaneously. From the multiplicity

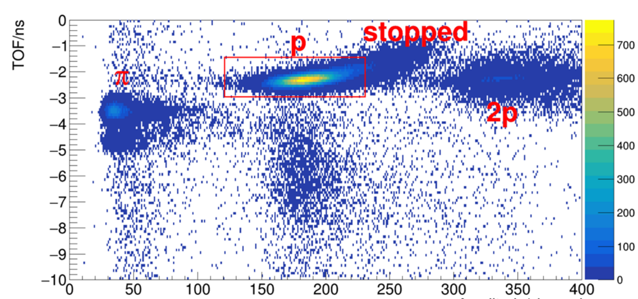

Fig. 14 (Color online) Scattering plot of the TOF signals and the energy loss in the scintillators

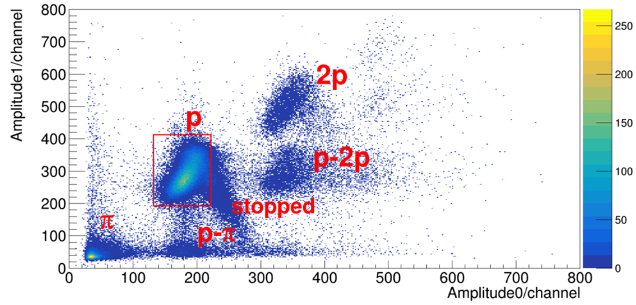

Fig. 15 (Color online) Scattering plot of the energy loss signals in the two scintillators

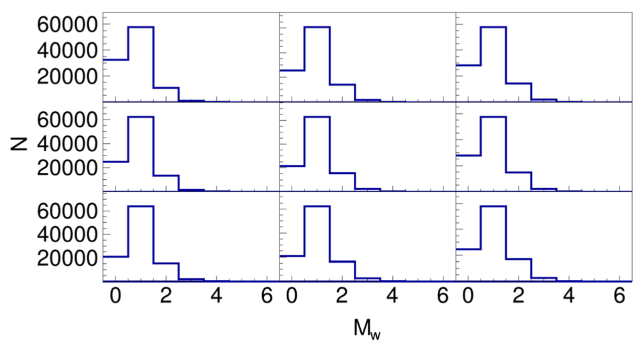

Fig. 16 (Color online) Fired wire multiplicity distribution in the 9 sense wire planes

distribution, with a threshold of $M_w \geq 1$, one can compute the efficiency of each layer, as summarized in Table 1. The average efficiency is between 70% and 80%, with an exception in the V1 wire plane. The firing efficiency is not high enough for the protons at this energy, because the working voltage is lowered to avoid the high leakage current arising from the high air humidity present at the time of the experiment (conducted in summer). In addition, one wire of the V1 layer is out of order, causing an even lower efficiency in this layer, as indicated in the third column in Table 1.

Unlike in the GEANT4 simulations, in the real test, the firing efficiency of each layer is less than 100%. Thus, the algorithm based on the simulation data has to be improved to overcome the inefficiency of the chambers. In particular, in the hit recognition, it is no longer required to have three wires being fired. The incident particle may only fire one or two wires in a certain chamber. Clearly, in order to construct a real track in three-dimensional space, the minimum hit multiplicity is 2, and the minimum wire multiplicity is 5. The multiplicity refers to the number of firing wires included in the candidate track. Using the improved searching method, the search efficiency was higher than 99%.

Figure 17 depicts the collinear characteristics of the hits in the three chambers. Panel (a) displays the schematic pattern of the fired wires viewed from different planes, e.g., the $X_\perp$ plane. The blue dotted lines represent the sense wire planes X of the three chambers, the red dots represent the fired wires in the candidate track, and the solid black lines represent the two track segments connecting fired wires in the first and second two chambers. It can be expected that the three fired wires viewed in the normal plane $X_\perp$, shall lie close to a straight line, and the angle between the two track segments satisfies $\alpha_{12} \approx 180^\circ$. The panel (b) of Fig. 17 presents the distribution of α_{12}. It is shown that the main peak appears in the vicinity of 180° with some discrete values on the left side. This is a natural broadening effect because the broadening of the beam spot is larger than the size of one single drift cell, and the drift length was not applied in this plot.

The tracking fitting algorithm for the data is the same as that in the simulation. However, in the experiment, the processing of the signal acquired by the flash ADC system has to be treated carefully. Digital signal filtering has been introduced to enhance the signal-to-noise ratio. The details of the technique are described in [43]. Furthermore, the relationship between the drift length L_d and the drift time T_d, which is determined by the time difference between the arrival of the signals of the drift chamber and scintillators, has to be calibrated before the fitting procedure. The calibration method is described in [31].

The results in Fig. 17 suggest that the track patterns are accurate and further track fitting can be processed. Because there are only three chambers and nine layers of sense wires, in order to access the tracking quality with the maximum redundancy, the tracks with nine wires fired, with one wire on each plane, are further selected to calculate the tracking residue, as shown in Fig. 18. Using a double Gaussian fit for the main peaks between ±1 mm, the weighted average of the standard deviations of the two Gaussian peaks is found to be 295 μm.

The uncertainty of 295 μm results from many sources of uncertainty, including those from the TOF broadening of the beam, the space-time relation, the signal distortion, and the mechanical accuracy in the assembly of the chamber. Except for the mechanical accuracy, all other terms, summing up to 150 μm [44], can be evaluated in the test of electronics and data analysis. For the mechanic accuracy, it

Table 1 Fired wire multiplicity of the 9 layers

Layer	X1	U1	V1	X2	U2	V2	X3	U3	V3
Efficiency	0.80	0.76	0.68	0.80	0.79	0.75	0.76	0.73	0.72

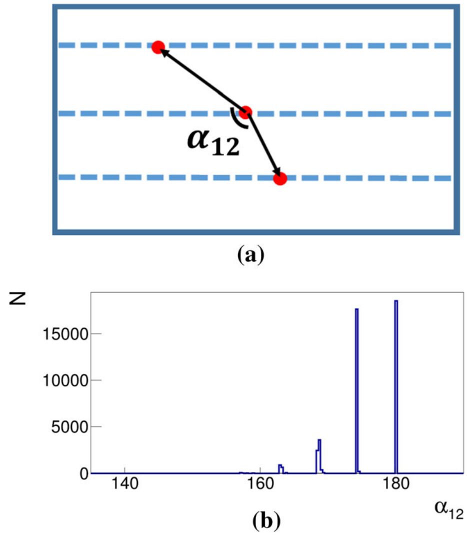

Fig. 17 (Color online) **a** Fired wire pattern in the perpendicular planes $X_{\perp}$, $U_{\perp}$, and $V_{\perp}$; **b** angle between the two track segments shown in (**a**)

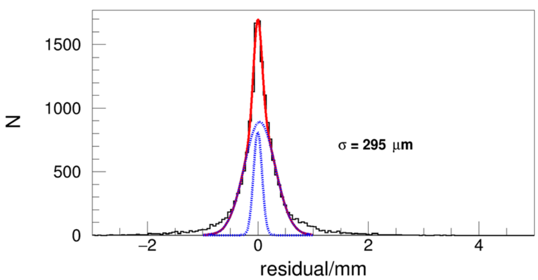

Fig. 18 (Color online) Track residue distribution for the tracks with nine wires fired. The blue dotted curves are the two Gaussian fits and the solid red curve is the sum

is found that, unlike in the calibration test where the displacement is reasonably small and can be corrected, the relative mechanical displacement of the wire planes is comparable with the residue. It is also found that the calibration of the displacement does not bring significant improvement. Therefore, it is very important to improve the mechanical assembling accuracy in the future mass production of chambers.

The redundancy of tracking is an important factor. Because there are three chambers in a row of the MWDC array prototype, there should be one layer of sense wire plane for a given orientation (X, U, or V) in each chamber to reduce the total number of electronic devices by 50%. The ability of tracking may not be influenced as predicted by the simulation. However, in real experiments, the redundancy of the tracking is reduced due to the non-perfectness of the detector or the signal, particularly for the tracks with a fired wire multiplicity of less than nine. Thus, we suggest resuming, as traditionally done, the design of two sense wire planes displaced by half the size of the drift cell for each direction of sense wire in each chamber.

4 Summary and outlook

Based on GEANT4 packages, the forward tracking system of the CEE was constructed, and the response of the detector was simulated. The tracking algorithm was developed for the MWDC system. A tracking residue of 29 μm and a momentum resolution of 4% were achieved in the simulation. A prototype of the tracking array consisting of three MWDCs with a sensitive area of 40×40 cm^2 and two scintillators as trigger detectors were built and tested using the proton beam at 400 MeV/u. Then, the firing efficiency was measured, and a tracking residue of 295 μm was achieved. Based on the prototype test, improvement in tracking redundancy and the mechanical assembly accuracy are suggested.

References

1. J.W. Xia, W.L. Zhan, B.W. Wei et al., The heavy ion cooler-storage-ring project (HIRFL-CSR) at Lanzhou. Nucl. Instr. Methods A **488**, 11 (2002). https://doi.org/10.1016/S0168-9002(02)00475-8
2. X.F. Luo, N. Xu, Search for the QCD critical point with fluctuations of conserved quantities in relativistic heavy-ion collisions at RHIC : an overview. Nucl. Sci. Tech. **28**, 112 (2017). https://doi.org/10.1007/s41365-017-0257-0
3. M.A. Stephanov, Sign of Kurtosis near the QCD critical point. Phys. Rev. Lett. **107**, 052301 (2011). https://doi.org/10.1103/PhysRevLett.107.052301
4. X. Luo et al., for STAR Collaboration, Energy dependence of moments of net-proton and net-charge multiplicity distributions at STAR. PoS **CPOD2014**, 019 (2015). https://doi.org/10.22323/1.217.0019
5. F. Gao, J. Chen, Y.X. Liu et al., Phase diagram and thermal properties of strong-interaction matter. Phys. Rev. D **93**, 094109 (2016). https://doi.org/10.1103/PhysRevD.93.094019
6. B.A. Li, L.W. Chen, C.M. Ko, Recent progress and new challenges in isospin physics with heavy-ion reactions. Phys. Rep. **464**, 113 (2008). https://doi.org/10.1016/j.physrep.2008.04.005
7. Z.G. Xiao, G.C. Yong, L.W. Chen et al., Probing nuclear symmetry energy at high densities using pion, kaon, eta and photon productions in heavy-ion collisions. Eur. Phys. J. A **50**, 37 (2014). https://doi.org/10.1140/epja/i2014-14037-6
8. P. Russotto, M.D. Cozma, A. Le Fevre et al., Flow probe of symmetry energy in relativistic heavy-ion reactions. Eur. Phys. J. A **50**, 38 (2014). https://doi.org/10.1140/epja/i2014-14038-5
9. J.M. Lattimer, A.W. Steiner, Constraints on the symmetry energy using the mass-radius relation of neutron stars. Eur. Phys. J. A **50**, 40 (2014). https://doi.org/10.1140/epja/i2014-14040-y
10. W.G. Newton, J. Hooker, M. Gearheart et al., Constraints on the symmetry energy from observational probes of the neutron star crust. Eur. Phys. J. A **50**, 41 (2014). https://doi.org/10.1140/epja/i2014-14041-x

11. L. Ou, Z.G. Xiao, H. Yi et al., Dynamic isovector reorientation of deuteron as a probe to nuclear symmetry energy. Phys. Rev. Lett. **115**, 212501 (2015). https://doi.org/10.1103/PhysRevLett.115.212501
12. B.P. Abbott et al., for LIGO collaboration, GW170817: Observation of gravitational waves from a binary neutron star inspiral. Phys. Rev. Lett. **119**, 161101 (2017). https://doi.org/10.1103/PhysRevLett.119.161101
13. B.P. Abbott et al., for LIGO collaboration, GW170817: measurements of neutron star radii and equation of state. Phys. Rev. Lett. **121**, 161101 (2018). https://doi.org/10.1103/PhysRevLett.121.161101
14. E.R. Most, L.R. Weih, J.S. Bielich, New constraints on radii and tidal deformabilities of neutron stars from GW170817. Phys. Rev. Lett. **120**, 261103 (2018). https://doi.org/10.1103/PhysRevLett.120.261103
15. Z.Y. Zhu, E.P. Zhou, A. Li, Neutron star equation of state from the quark level in light of GW170817. AstroPhys. J. **862**, 98 (2018). https://doi.org/10.3847/1538-4357/aacc28
16. F.J. Fattoyev, J. Piekarewicz, C.J. Horowitz et al., Neutron skins and neutron stars in the multimessenger era. Phys. Rev. Lett. **120**, 172702 (2018). https://doi.org/10.1103/PhysRevLett.120.172702
17. F. Fu, Z.G. Xiao, Y.P. Zhang et al., Nuclear stopping and compression in heavy-ion collisions at intermediate energies. Phys. Lett. B **666**, 359 (2008). https://doi.org/10.1016/j.physletb.2008.07.063
18. W. Reisdorf et al., for FOPI Collaboration, Nuclear stopping from 0.09 A to 1.93 A GeV and its correlation to flow. Phys. Rev. Lett. **92**, 232301 (2004). https://doi.org/10.1103/PhysRevLett.92.232301
19. M. Zhang, Z.G. Xiao, B.A. Li et al., Systematic study of the π^-/π^+ ratio in heavy-ion collisions with the same neutron/proton ratio but different masses. Phys. Rev. C **80**, 034616 (2009). https://doi.org/10.1103/PhysRevC.80.034616
20. L.M. Lyu, H. Yi, Z.G. Xiao et al., Conceptual design of the HIRFL-CSR external-target experiment. Sci. China Phys. Mech. Astron. **60**, 012021 (2017). https://doi.org/10.1007/s11433-016-0342-x
21. W. Huang, F. Lu, H. Li et al., Laser test of the prototype of CEE time projection chamber. Nucl. Sci. Tech. **41**, 29 (2018). https://doi.org/10.1007/s41365-018-0382-4
22. D. Hu, X. Wang, M. Shao et al., Beam test study of the MRPC-based T0 detector for the CEE. J. Instrum. **14**(09), C09030 (2019). https://doi.org/10.1088/1748-0221/14/09/C09030
23. D. Hu, M. Shao, Y. Sun et al., A T0 trigger detector for the external target experiment at CSR. J. Instrum. **12**(06), C06010 (2017). https://doi.org/10.1088/1748-0221/12/06/C06010
24. Q. Zhang, D. Han, P. Lyu et al., Performance of high rate MRPC with different gas mixtures. J. Instrum. **14**(01), P01003 (2019). https://doi.org/10.1088/1748-0221/14/01/P01003
25. X.L. Chen, D. Han, M. Gouzevitch et al., Study of MRPC performance at different temperatures. J. Instrum. **13**(12), P12005 (2018). https://doi.org/10.1088/1748-0221/13/12/P12005
26. P. Lyu, D. Han, Y. Wang et al., Performance study of a real-size mosaic high-rate MRPC. J. Instrum. **13**(06), P06016 (2018). https://doi.org/10.1088/1748-0221/13/06/P06016
27. P. Lyu, Y. Wang, B. Guo et al., Development and performance of self-sealed MRPC. J. Instrum. **12**(03), C03055 (2017). https://doi.org/10.1088/1748-0221/12/03/C03055
28. P. Lyu, Y. Wang, B. Guo et al., Gas related effects on multi-gap RPC performance in high luminosity experiments. J. Instrum. **11**(11), C11041 (2016). https://doi.org/10.1088/1748-0221/11/11/C11041
29. Y.Z. Sun, Z.Y. Sun, S.T. Wang et al., The drift chamber array at the external target facility in HIRFL-CSR. Nucl. Instr. Methods A **72**, 894 (2018). https://doi.org/10.1016/j.nima.2018.03.044
30. S.W. Tang, S.T. Wang, L.M. Duan et al., A tracking system for the external target facility of CSR. Nucl. Sci. Tech. **28**, 68 (2017). https://doi.org/10.1007/s41365-017-0217-8
31. H. Yi, Z. Zhang, Z.G. Xiao et al., Prototype studies on the forward MWDC tracking array of the external target experiment at HIRFL-CSR. Chin. Phys. C **38**, 126002 (2014). https://doi.org/10.1088/1674-1137/38/12/126002
32. Z. Wang, S. Zou, Y. Fan et al., A beam monitor using silicon pixel sensors for hadron therapy. Instr. Methods A **20**, 849 (2017). https://doi.org/10.1016/j.nima.2016.12.050
33. L. Zhao, L.F. Kang, J.W. Zhou, A 16-Channel high-resolution time and charge measurement module for the external target experiment in the CSR of HIRFL. Nucl. Sci. Tech. **25**, 010401 (2014). https://doi.org/10.13538/j.1001-8042/nst.25.010401
34. P. Deng, L. Zhao, J. Lu et al., Readout electronics of T0 detector in the external target experiment of CSR in HIRFL. IEEE Trans. Nucl. Sci. **1315**, 65 (2018). https://doi.org/10.1109/TNS.2018.2834426
35. L. Zhao, L. Kang, M. Li et al., The prototype readout electronics system for the External Target Experiment in CSR of HIRFL. J. Instrum. **9**(07), C07003 (2014). https://doi.org/10.1088/1748-0221/9/07/C07003
36. L.S. Zhan, L. Zhao, L.F. Kang, et al. The Clock System in Readout Electronics System for the External Target Experiment in CSR of HIRFL, in *International Conference on Computer Information Systems and Industrial Applications*. Atlantis Press, (2015). https://doi.org/10.2991/cisia-15.2015.86
37. G. Charpak, R. Bouclier, T. Bressani et al., The use of multiwire proportional counters to select and localize charged particles. Nucl. Instr. Methods A **262**, 62 (1968). https://doi.org/10.1016/0029-554X(68)90371-6
38. Geant4 Collaboration. Book For Application Developers. Rev1.0: Dec 8th (2017)
39. W. Reisdorf, A. Andronic, R. Averbeck et al., Systematics of central heavy ion collisions in the 1AGeV regime. Nucl. Phys. A **848**, 366 (2010). https://doi.org/10.1016/j.nuclphysa.2010.09.008
40. H. Bischof, R. Fruhwirth, Recent developments in pattern recognition with applications in high-energy physics. Nucl. Instr. Methods A **419**, 259 (1998). https://doi.org/10.1016/S0168-9002(98)00798-0
41. J. Smyrski, Ch. Kolf, H.-H. Adam et al., Drift chamber with a c-shaped frame. Nucl. Instr. Methods A **541**, 574 (2005). https://doi.org/10.1016/j.nima.2004.12.006
42. W.J. Cheng, Z. Zhang, H. Yi et al., Development of a fan-in and delay module for MWDC based on Flash-ADC acquisition scheme. Nucl. Tech. **39**, 040403 (2016). https://doi.org/10.11889/j.0253-3219.2016.hjs.39.040403. (in Chinese)
43. H. Yi, L.-M. Lu, Z. Zhang et al., A Flash-ADC data acquisition system developed for a drift chamber array and a digital filter algorithm for signal processing. Chin. Phys. C **40**, 116102 (2016). https://doi.org/10.1088/1674-1137/40/11/116102
44. H. Yi, Doctoral Thesis, Tsinghua University (2017) (in Chinese)